TECHNICAL PAPER

Comparison of microstructure and mechanical performance of laser and electron beam welded Ti6Al4V alloy

Sohini Chowdhury[1] · N. Yadaiah[1] · M. Murlidhar[1] · Deepati Anil Kumar[2] · C. P. Paul[3,4] · S. K. Patra[5] · Sunpreet Singh[6] · Grzegorz Królczyk[7] · Chander Prakash[8]

Abstract

Laser beam welding and electron beam welding are the most recent joining technologies that interface engineering and physics concepts. The present research work focuses on the comparison of the microstructural and mechanical performances of Ti6Al4V, an alloy that displays sensible weldability owing to high susceptibility to oxidation process at elevated temperature, welded joints by using laser and electron beam welding. The as-welded alloy has been examined to study the effect of similar heat input conditions and focal point positions on butt-joint Ti6Al4V specimens in response of the weld morphology, microstructural feature, micro-hardness distribution and angular deformation. The results indicated that electron beam welding process is more appropriate and favorable to join Ti6Al4V alloy specimens and full penetrated electron beam weld joint is procured without any defects. However, narrow weld seam with refined grain structures is developed in the weld zone of laser beam welded specimens. Also, defocusing the beam position by -1 mm contributed to grain refinement in the weld zone of laser and electron beam welded specimens. Moreover, the magnitude of micro-hardness distribution in the weld zone of laser beam weldments is higher than electron beam weldments by 0.66 times. However, the micro-hardness magnitude is substantially enhanced by 32% and 16% for laser and electron beam weldments, respectively, due to negative defocusing beam position. From the results, it is determined that the magnitude of angular deflection is higher for laser beam weldments than electron beam weldments due to higher difference in fusion zone areas across the neutral axis. Moreover, angular deflection magnitude in electron and laser beam weldments is lowered by 15.8% and 7.4%, respectively, due to negative defocusing beam position.

Keywords Laser beam welding (LBW) · Electron beam welding (EBW) · Ti6Al4V alloy · Metallographic analysis · Focal point position (FPP) · Angular deformation

Technical Editor: Izabel Fernanda Machado.

✉ N. Yadaiah
ny@nerist.ac.in

✉ Chander Prakash
chander.mechengg@gmail.com

1 Department of Mechanical Engineering, North Eastern Regional Institute of Science and Technology (NERIST), Nirjuli, Arunachal Pradesh 791109, India

2 Department of Mechanical and Maintenance Technology, CAIT, Jazan University, Jizan, Kingdom of Saudi Arabia

3 Laser Development and Industrial Applications Division, Raja Ramanna Centre for Advanced Technology, Indore, Madhya Pradesh 452013, India

4 Homi Bhabha National Institute, BARC Training School Complex, Mumbai, Maharashtra 400085, India

5 Sukhoi Engine Division, Hindustan Aeronautics Limited-Koraput, Sunabeda, Odisha 763002, India

6 Department of Mechanical Engineering, National University of Singapore, Singapore, Singapore

7 Department of Mechanical Engineering, Opole University of Technology, 76 Proszkowska St., 45-758 Opole, Poland

8 School of Mechanical Engineering, Lovely Professional University, Phagwara, Punjab 144411, India

1 Introduction

Ti6Al4V ($\alpha + \beta$) two-phase alloy is primarily employed in applications where its distinctive characteristics substantiate the selection standards. The unique integration of high stiffness and strength, low ductility and excellent corrosion- and heat-resistant properties has marked titanium alloys in diverse domains of aviation, petrochemical, nuclear and automobile [1]. Moreover, the physical and mechanical characteristics of Ti6Al4V alloy can be improved by controlling alloy composition and microstructural growth during thermal and mechanical processing.

In the recent past, various fusion and solid-state joining processes have been established to join Ti6Al4V alloy parts. However, the fusion welding operations are fundamentally carried out in an inert or vacuum condition since Ti6Al4V alloy is highly subjected to embrittlement when exposed to atmospheric elements at extreme temperatures. Therefore, obtaining Ti6Al4V alloy joints of sound weld integrity by using an appropriate welding procedure is an elemental operation. However, fabricating titanium alloy specimens using conventional fusion welding methodologies has resulted in poor mechanical characteristics due to improper shielding measures [2]. Thus, advanced and efficient welding techniques such as laser beam welding (LBW) [3–5], electron beam welding (EBW) [6and7], hybrid welding [8] and friction stir welding (FSW) [9and10] have been introduced and employed to weld Ti6Al4V alloy parts successfully.

To identify the most desirable and suitable welding approach from existing joining techniques, several comparative studies are presented based on microstructural and mechanical characteristics of Ti6Al4V alloy. Yulian et al. [11] reported that titanium sheets welded by EBW operation yielded finer grains and better mechanical characteristics when compared with gas tungsten arc (TIG) weldments. Gao et al. [12] revealed that pulsed Nd:YAG laser welding operation is more appropriate to weld Ti6Al4V alloy plates than TIG welding operation. Meshram and Mohandas [13] investigated the influence of friction and EBW operations on microstructural and mechanical characteristics of near-α titanium alloy. They observed that electron beam weld joints exhibited higher strength, stress rupture and creep resistance property than friction stir weld joints. Also, the influence of welding methods, viz. LBW and laser–MIG hybrid welding (LAMIG), on joint properties and mechanical characteristics of titanium alloy is carried out. They concluded that LAMIG operation is more feasible and sustainable than LBW operation. Also, LAMIG
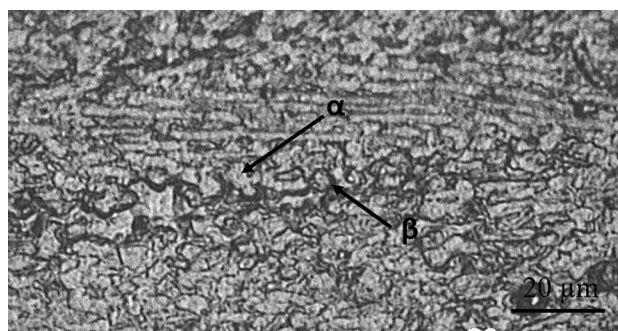

Fig. 1 Microstructure of as-received Ti6Al4V alloy base plate

welded joints exhibited superior mechanical properties than laser welded joints [14]. All these experimental efforts are focused to determine feasible welding approach for successful Ti6Al4V alloy weld joint. However, laser beam and electron beam welding techniques are the most flexible joining methods to weld Ti6Al4V alloy since it offers controlled beam energy with high precision and efficacy and eliminates the requirement of any filler metal.

Although several studies have established the fact that laser and electron beam welding processes are suitable joining procedures to weld Ti6Al4V alloy metals, a comparative analysis of laser and electron beam welding methods under same heat input conditions is indeed a requirement to comprehend the most preferable joining technique. Therefore, the present work is aimed at differential examination of laser and electron beam welded Ti6Al4V alloy plates of 3 mm thickness in butt-joint orientation. The influence of heat input conditions and focal point positions for two different welding methods is examined with respect to weld geometry, microstructural and mechanical characteristics. Moreover, the weld integrity of Ti6Al4V alloy joints is examined by micro-hardness and residual deformation.

2 Materials and experimental procedure

In the present study, laser and electron beam welding experiments were carried out on milled–annealed Ti6Al4V alloy plates in butt-joint configuration having dimensions of 50 mm × 25 mm × 3 mm. The chemical composition of as-received Ti6Al4V alloy base plate is presented in Table 1. The microstructure of as-received Ti6Al4V alloy base plate is represented in Fig. 1. The crystallographic arrangement of Ti6Al4V alloy base plate reveals a bimodal structure in which primary α grains (hexagonal

Table 1 Chemical composition of as-received Ti6Al4V alloy base plate

Element	Al	V	C	O	Fe	Ti
Wt(%)	5.4	3.8	0.08	0.3	0.25	Bal

close-packed structure) are enclosed by β grains (body-centered cubic structure). Average diameter of primary α and β grains of Ti6Al4V alloy base metal is 22.4 μm and 18.2 μm, respectively.

The laser welding experiments were conducted on a 2.0 kW ytterbium laser system (YLS) which is integrated with a computerized numerically controlled (CNC) controller, CNC workstation and laser processing head. The laser processing head was mounted perpendicular to the work station, and the focal length was adjusted to 230 mm such that a minimum spot diameter of 0.2 mm was obtained. The CNC workstation controlled the transverse and horizontal movement of the base plates. Moreover, argon gas of 99.99% purity was delivered from the side nozzle such that it made an angle of 45° with the laser beam.

The electron beam welding experiments were conducted on a Techmeta Lara 52 electron beam machine which comprises a numerically controlled welding chamber, a triode electron gun, a CNC controller and a vacuum system. The focus current was set at 2030 mA such that a minimal electron beam diameter of 0.3 mm was attained. The worktable inside the welding chamber was controlled by a CNC controller which can transverse across longitudinal and horizontal motion. The welding chamber is vacuumized at 10^{-5} mbar using a vacuum pump prior to welding operation. The actual welding system and the schematic of experimental setup corresponding to both the welding processes are represented in Fig. 2. The experimental conditions of ytterbium fiber laser welding machine and electron beam welding machine are listed in Table 2.

Prior to joining operations, Ti6Al4V alloy base plates were wiped with ethanol, arranged in butt-joint orientation on a traditional designed fixture such that zero-gap tolerance is maintained. The same fixture is utilized for both the welding methods, and it comprises clamping plate and work plate. The components of fixture are made of aluminum alloy which ensures minimum angular deformation of plates [15]. The fixture is then placed longitudinally on the worktable of welding systems and aligned vertically to the laser head and electron beam gun. The laser beam supply and inert gas supply are controlled by on/off mode which is provided in laser workstation. The electron beam supply and vacuum supply are controlled by CNC controller and power supply unit. The processing conditions of LBW and EBW operations are listed in Tables 3 and 4, respectively. It can be identified from Tables 3 and 4 that a constant linear energy condition is maintained corresponding to each processing criterion of laser and electron beam welding methods. Moreover, negative defocusing is incorporated in both the welding processes to examine its impact on weld geometry and characteristics. The negative defocusing is attained by changing the focusing distance of laser and electron beam with respect to the upper surface of the substrate.

After joining operations, angular deformation pattern of laser and electron beam welded Ti6Al4V alloy samples is examined using a height Vernier gauge. The measuring accuracy is 0.01 mm. An average value of angular deformation is determined across the weldment of Ti6Al4V alloy at three distinct longitudinal positions. Henceforth, the butt-joint Ti6Al4V alloy samples are sectioned perpendicular to the weld joint and polished with emery papers of grit size 120 grade to 2000 grade. Thereafter, weld samples are polished on Velvet cloth and swabbed with Kroll's reagent solution for metallographic examination. The weld geometry and weld microstructures of laser and electron beam welded Ti6Al4V alloy samples are obtained using an optical microscopy. Also, average grain size of Ti6Al4V alloy weld samples corresponding to laser and electron beam welding methods is determined using ImageJ software.

Vicker's micro-hardness test is conducted for Ti6Al4V alloy weld samples using an indentation load of 500 g for a dwell time of 20 s. The micro-hardness distribution is examined from the weld zone interface to the base metal at an interval of 0.5 mm and below 0.25 mm from the weld surface. The micro-hardness value is obtained directly from the test indicator of Vicker's hardness machine.

3 Results and discussion

The differential influence of laser and electron beam welding conditions is examined for 3-mm-thick butt-joint Ti6Al4V alloy plates relative to macro- and microstructural analysis, micro-hardness distribution and angular deformation state. The present analysis is carried out for a wide range of heat input conditions such that weld penetration is varied from partial penetration to full penetration and focusing state of laser and electron beam is adjusted at 0 mm and − 1 mm.

3.1 Metallographic analysis

The differential influence of fiber laser and electron beam welding methods under same heat input condition and FPP is examined with respect to macro–microstructural characteristics, thermally induced distortion and micro-hardness distribution. Figure 3 shows the top surface appearance of Ti6Al4V alloy weld joint processed by laser and electron beam welding methods at 112.5 J mm^{-1}. It can be recognized that the weld surfaces are regular and smooth corresponding to both the joining processes. However, the surface width of electron beam weldment is higher relative to laser beam weldment. Moreover, weld groove is also identified along the edges of electron beam welded Ti6Al4V alloy sample (Fig. 3b).

The cross-sectional macrograph of Ti6Al4V alloy specimens corresponding to both the welding processes is

Fig. 2 a 2 kW Ytterbium fiber laser welding system; **b** schematic of laser beam welding setup; **c** TECHMETA LARA 52 electron beam welding system; and **d** schematic of electron beam welding process in vacuum chamber
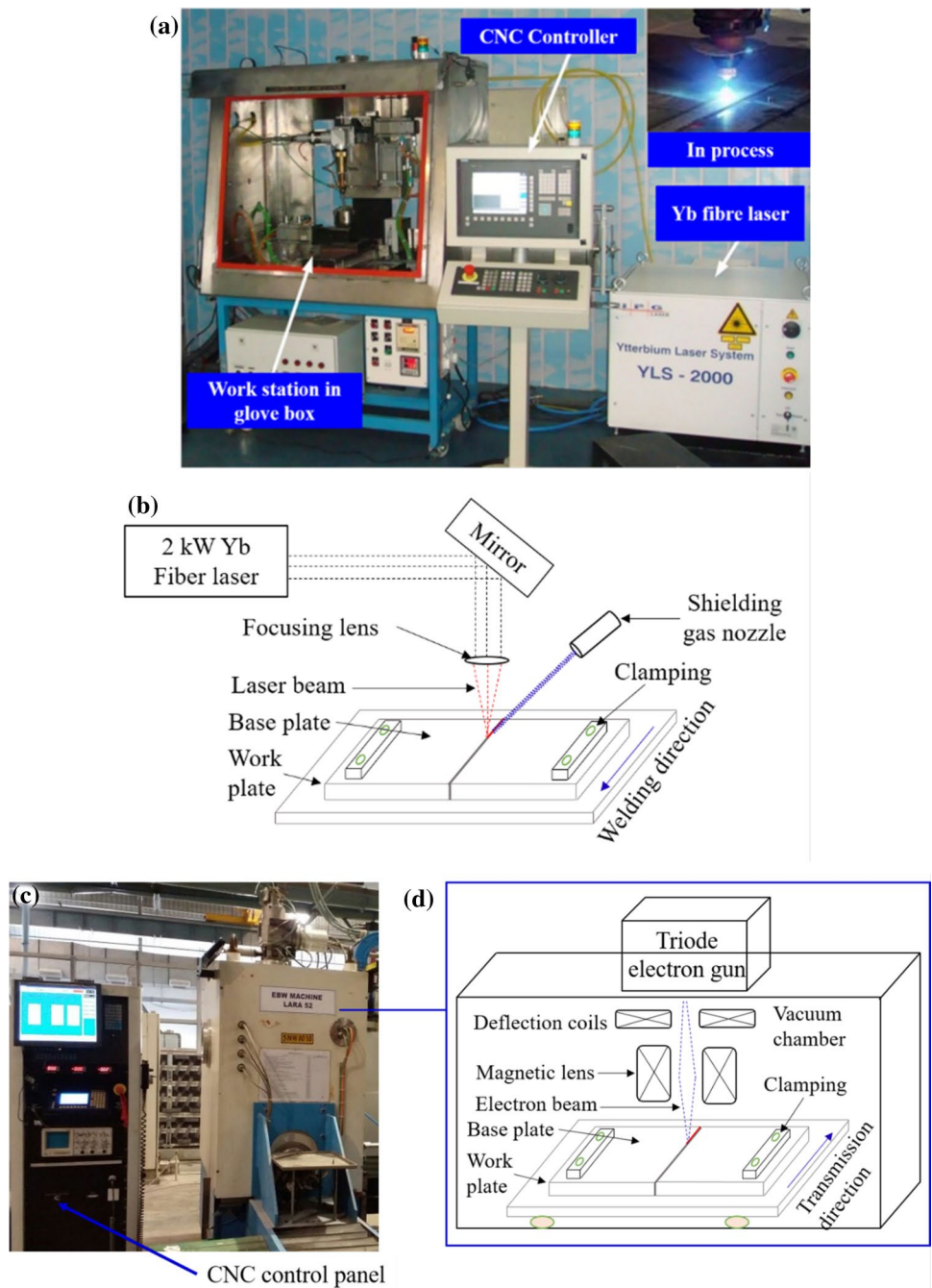
Table 2 Experimental conditions of ytterbium fiber laser welding and electron beam welding machine

Ytterbium fiber laser welding		Electron beam welding	
Laser power mode	Continuous wave	Electron gun category	Triode
Beam mode	Flat top surface and multi-mode	Maximum electron beam power	10 kW
Wavelength	1080 nm	Accelerating voltage range	20 to 60 kV
Spot diameter	200 μm	Electron beam current range	0 to 167 mA
Beam angle	90°	Vacuum range	10^{-5} to 10^{-7} mbar
Inert gas	Argon	Electron beam deflection angle range	0 to 6°
Fiber core diameter	50 μm	Electron beam diameter	300 μm

Table 3 Processing conditions of LBW operation

Weld sample	Power (W)	Scan speed (m min^{-1})	Focal point position (mm)	Heat input per unit length (J mm^{-1})
L1 and L2	1500	0.8	0 and − 1	112.5
L3 and L4	1350	0.7	0 and − 1	115.71
L5 and L6	1200	0.6	0 and − 1	120
L7 and L8	1700	0.7	0 and − 1	145.71

Table 4 Processing conditions of EBW operation

Weld sample	Accelerating voltage (kV)	Beam current (mA)	Scan speed (m min^{-1})	Focal point position (mm)	Heat input per unit length (J mm^{-1})
E1 and E2	60	25	0.8	0 and -1	112.5
E3 and E4	50	27	0.7	0 and -1	115.71
E5 and E6	50	24	0.6	0 and -1	120
E7 and E8	60	28.33	0.7	0 and -1	145.71

Fig. 3 Top surface appearance of Ti6Al4V alloy joint welded by **a** LBW process and **b** EBW process at 112.5 J mm^{-1}
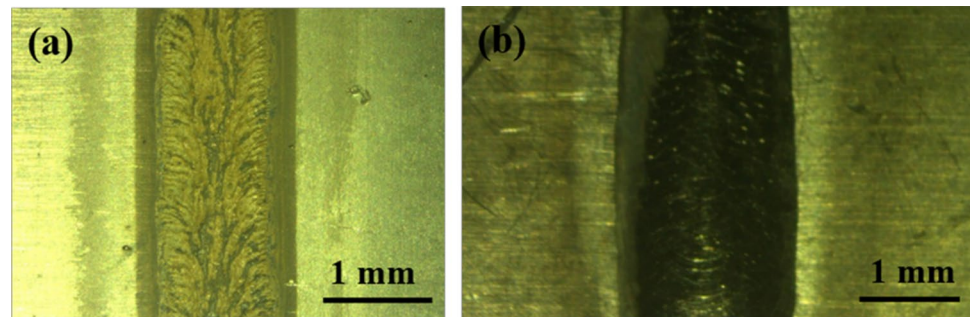
presented in Fig. 4. Ti6Al4V alloy samples joined by laser and electron beam welding techniques displayed a nail-head profile and a conical profile. The variation in laser and electron beam welds corresponding to same heat input condition is primarily due to difference in physical parameters such as surface tension force, recoil pressure, vapor pressure, gravity and phase transformation and volume contraction during welding and solidification processes [16, 17]. Moreover, the difference in penetration level and weld width is clearly identified corresponding to laser and electron beam welds processed under constant heat input condition and at focused and defocused beam condition. This phenomenon is due to higher energy conversion efficiency (~85%) of EBW process [18]. Therefore, a full penetration is witnessed in all the electron beam welds. However, the weld penetration in laser welded samples is observed to increase from partial penetration to full penetration with an increase in thermal energy input. Also, from Fig. 4(a) and (c), it is witnessed that a higher bead width is attained in electron beam weldments when compared with laser beam weldments. This phenomenon is primarily due to transmission of thermal energy in transverse direction once complete weld penetration is obtained. Besides, pores are observed in laser welded Ti6Al4V alloy samples near the interface of weld zone and heat-affected zone. The pores are generated on account of atmospheric gases dissolved in the melt pool during the welding process which is not released during the solidification process. Also, such similar observations were reported by Li et al. [19] and Li et al. [20].

A slightly increased weld width is determined in laser and electron beam welds processed with negative defocused beam position (Fig. 4b and d). The negative defocusing beam position facilitates material–beam interaction below the substrate surface and an increased energy distribution over the substrate surface. Hence, a wider weld area is obtained due to application of negative defocusing position of laser and electron beam. Moreover, the effect of undercut is more pronounced in electron beam welds due to high thermal energy delivered to the substrate.

The crystallographic development in the FZ and HAZ of Ti6Al4V alloy is quite different, and it depends on melting and solidification behavior. The FZ of electron beam welded

Fig. 4 Weld macrographs of Ti6Al4V alloy joints at different heat input conditions and FPPs: **a** 112.5 J mm^{-1} and 0 mm FPP, **b** 112.5 J mm^{-1} and -1 mm FPP, **c** 120 J mm^{-1} and 0 mm FPP and **d** 120 J mm^{-1} and − 1 mm FPP
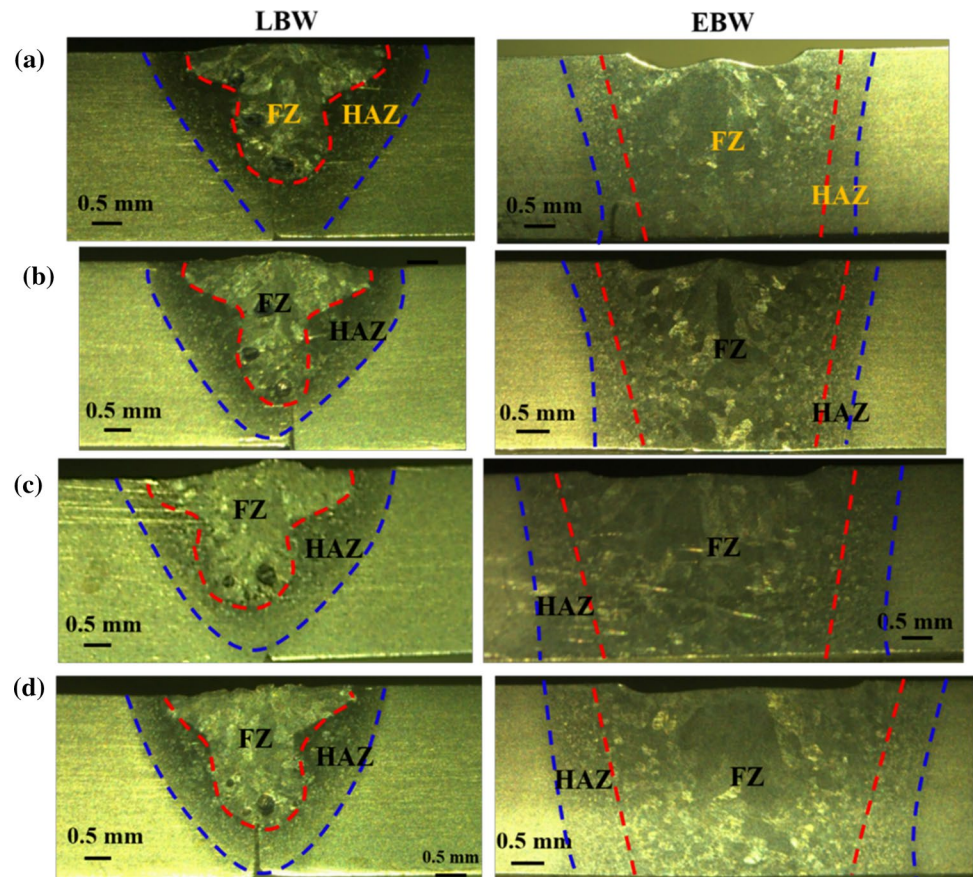

Ti6Al4V alloy samples undergoes complete melting and solidification process. Moreover, the rate of solidification process in the FZ governs the microstructural evolution and weld quality. However, the HAZ does not undergo melting process and it experiences significant temperature gradient, which results in solid-state microstructural transformation. Hence, the integrity of weld joint is primarily governed by the size of the grains and its distribution in FZ and HAZ.

The fusion zone microstructure of Ti6Al4V alloy weld metal joined by electron and laser beam welding process at 112.5 J mm^{-1} is presented in Fig. 5. The weld metal is characterized by martensitic α^1 platelets and dense acicular α^1 martensitic needles, which is illustrated in Fig. 5a and b. The difference in microstructural characteristics in the FZ at constant heat input condition corresponding to laser and electron beam welding processes is attributed to the solidification rate. The weld sample corresponding to E1 of Table 4 undergoes a relatively slower solidification process during EBW process. As a result, acicular α^1 phases of higher width and plate-like morphology are evolved in the FZ instead of acicular α^1 needles (Fig. 5a). On the contrary, the weld sample corresponding to L1 of Table 3 encounters a faster solidification process during LBW process (Fig. 5b). Hence, acicular α^1 martensitic phases of lower width are formed in the weld zone. However, for negative defocusing beam

position, the microstructural characteristics are quite distinct at the weld zone, which is represented in Fig. 5(c) and (d). The electron beam weld microstructure (Fig. 5c) exhibits refined lamellar α^1 structures of acicular morphology within a basket-weave matrix along with retained β phases. The presence of lamellar α^1 structures in the FZ reflects that the solidification process due to negative beam defocusing is relatively faster as compared to focused beam condition, while the fusion zone microstructure corresponding to weld sample number L2 of Table 3 (Fig. 5d) shows the presence of fine equiaxed acicular α^1 needles in β phases of lesser density. Therefore, based on the results it can be suggested that the solidification process in the FZ associated with LBW technique is higher when compared with EBW technique. And, the solidification rate associated with negative defocusing beam position is determined to be faster than focused beam condition.

The optical micrographs of laser and electron beam weld joints at FZ corresponding to 115.71 J mm^{-1} are presented in Fig. 6. The microstructure of electron beam welded Ti6Al4V alloy (Fig. 6a) shows the presence of equiaxed acicular α^1 needles distributed along with small quantity of retained β phases, while the micrograph (Fig. 6b) of laser beam weld at focused state displays the existence of only acicular α^1 needles along unique direction in β phase. Though, the fraction

Fig. 5 FZ microstructure of Ti6Al4V alloy weld metal processed at 112.5 J mm⁻¹ by **a** EBW process at 0 mm FPP, **b** LBW process at 0 mm FPP, **c** EBW process at − 1 mm FPP and **d** LBW process at − 1 mm FPP
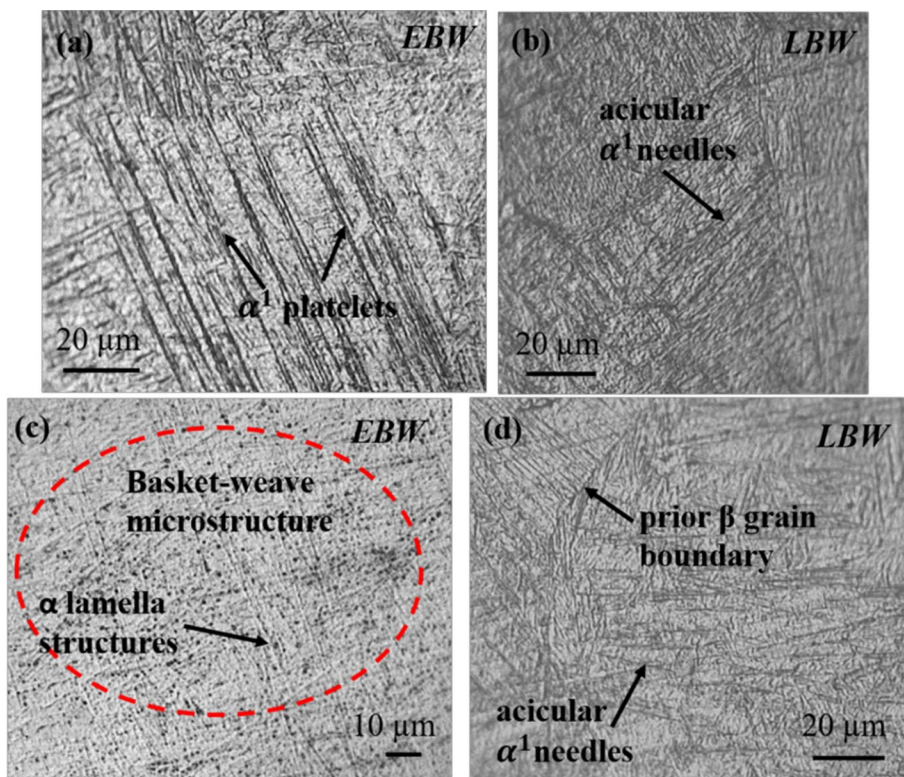
Fig. 6 FZ microstructure of Ti6Al4V alloy weld metal processed at 115.71 J mm⁻¹ by **a** EBW process at 0 mm FPP, **b** LBW process at 0 mm FPP, **c** EBW process at -1 mm FPP and **d** LBW process at − 1 mm FPP
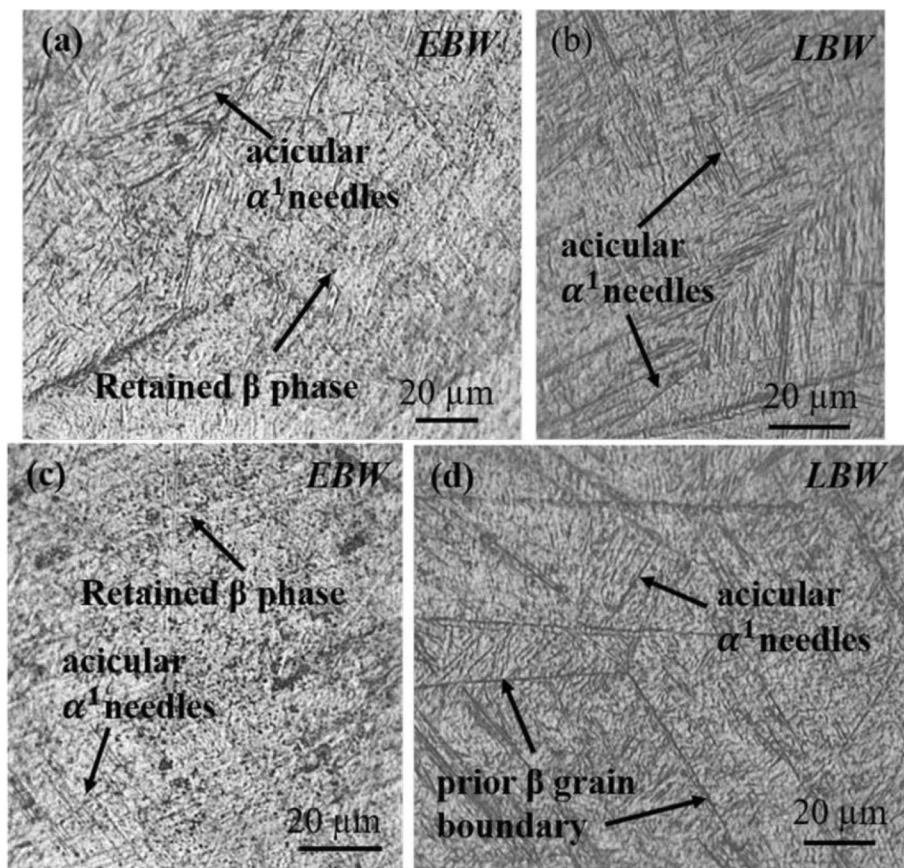
content of retained β phases in the FZ of electron beam welds (Fig. 6c) is determined to be more pronounced due to application of negative defocusing beam condition. Moreover, the width of martensitic α^1 phases in the weld zone corresponding to negative defocused beam state is evaluated to be shorter as against those joined at focused state of electron beam. The microstructure of laser beam weld joint at FZ for negative defocusing beam position is presented in Fig. 6(d). The evolution of acicular martensitic phases within prior β grains is directional, and it displays shorter crystal size when evaluated against focused beam condition (Fig. 6b). Based on the crystallographic arrangement in electron and laser beam welds at 115.71 J mm^{-1}, it is observed that FZ mainly comprises martensitic α^1 phases. However, a significant percentage content of retained β phase is determined in electron beam welds due to slower solidification process in the FZ. Hence, it is expected that the presence of β phases in the FZ will lower the micro-hardness magnitude across the weld joint.

The optical microstructure of electron and laser beam welds at 115.71 J mm^{-1} and different FPP is shown in Fig. 7. The micrograph illustrates FZ and HAZ, and it can be observed that the FZ of electron and laser beam welds are distinguished by dense dark-colored region, whereas HAZ is identified by light-colored region. The dense area in the FZ is primarily due to the evolution of dense acicular martensitic phase within the boundary of prior β grains. Moreover, the fraction content of acicular martensitic structures declines sharply from the FZ boundary toward HAZ and

base metal. Therefore, HAZ is primarily recognized by a lighter toned area.

The microstructure of electron and laser beam welds at the center of HAZ corresponding to negative defocused and focused beam condition is presented in Fig. 8. The microstructure of electron beam welds joined with negative defocused and focused beam condition (Fig. 8a and b) shows the presence of acicular α^1 needles with significant amount
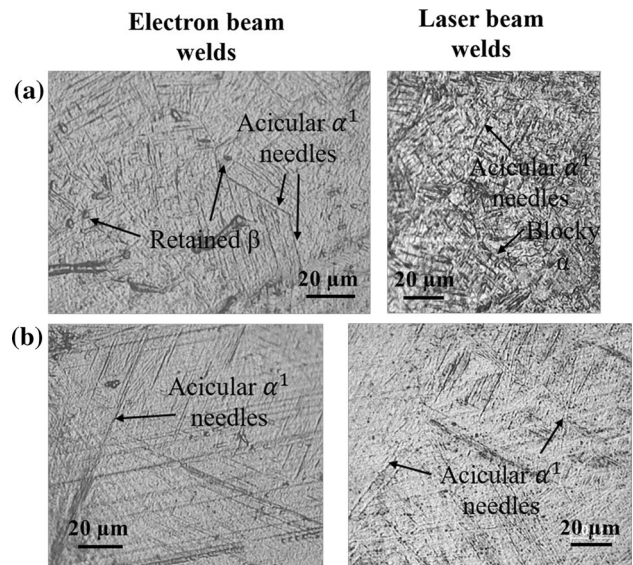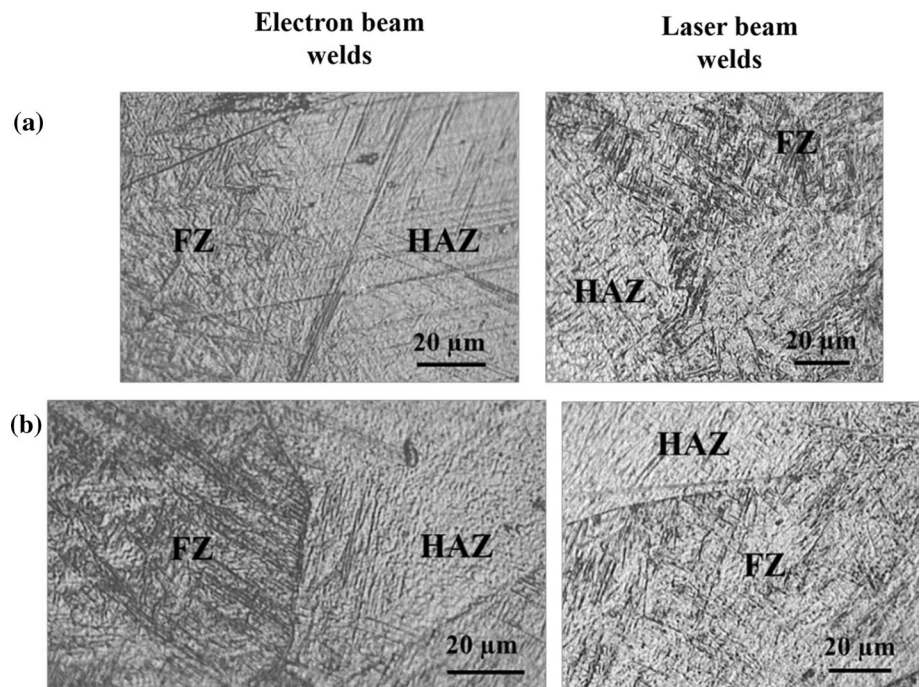

Fig. 8 FZ microstructure of laser and electron beam welds at HAZ center processed at 115.71 J mm^{-1} corresponding to **a** -1 mm FPP and **b** 0 mm FPP

Fig. 7 Optical micrographs of electron and laser beam welds at 115.71 J mm^{-1} corresponding to FPP **a** -1 mm and **b** 0 mm

of β traces. The existence of aciculate martensitic structures at the center of HAZ depicts that the peak temperature underwent far beyond β transus temperature (995 °C). The micrograph of laser beam weld joined at -1 mm FPP is represented in Fig. 8(a). It comprises blocky α along with aciculate α^1 needles of lower width. The appearance of blocky α signifies that the HAZ experienced peak temperature between β transus temperature and liquidus temperature (1655 °C). Similarly, the microstructure of Ti6Al4V alloy weldment joined at 0 mm FPP (Fig. 8b) exhibits martensitic α^1 needles with few traces of β phase. From these results, it can be stated that the HAZ undergoes different temperature transitions corresponding to focused and defocused laser and electron beam position. The HAZ experiences distinct temperature gradient unlike FZ and undergoes solid-state microstructural transformation. For laser beam welding process, at focused beam condition the HAZ experienced a slightly higher temperature gradient or higher solidification rate than at defocused beam condition. Hence, HAZ microstructure at focused beam condition revealed the existence of martensitic α^1 needles along with β grains and no traces of blocky α. However, for electron beam weldments the HAZ experienced almost same temperature gradient at HAZ center. Therefore, the HAZ microstructure exhibited almost grain characteristics.

3.2 Micro-hardness distribution

The Vickers micro-hardness distribution plot across the weld joint of laser and electron beam welds at 112.5 J mm^{-1} is presented in Fig. 9 for two different focal point positions. The hardness property in Ti6Al4V alloy is directly proportional to the fraction content of acicular martensitic phase in different weld zones. Hence, the magnitude of micro-hardness is determined to be highest in the FZ followed by HAZ and base metal for electron and laser beam welds. The maximum micro-hardness magnitude in the FZ corresponding to electron and laser beam welds is 324 HV and 392 HV at 0 mm FPP and 350 HV and 387 HV at -1 mm FPP. Moreover, maximum micro-hardness magnitude in the HAZ

for electron and laser beam welds is evaluated as 299.3 HV and 313.3 HV at 0 mm FPP and 334.7 HV and 355.4 HV at -1 mm FPP, respectively. Furthermore, from Fig. 9(a) and (b), it is evaluated that the average micro-hardness distribution in the FZ of electron beam welds is 0.66 times the average micro-hardness magnitude of laser beam welds. The increased micro-hardness magnitude in laser beam welds is on account of faster solidification process which leads to the evolution of fine aciculate martensitic phases in the FZ. In addition, due to negative defocused beam position of laser and electron beam, the crystal size in the weld zone is reduced significantly and becomes refined. Hence, the average magnitude of micro-hardness in the weld zone corresponding to defocused beam condition for laser and electron beam welds is enhanced by 32% and 16%, respectively.

Figure 10 presents the average micro-hardness magnitude of laser and electron beam welds corresponding to different heat input conditions and FPP as given in Tables 3 and 4. The hardness value decreases with an increase in heat input per unit length, since FZ microstructure exhibited coarse martensitic α^1 structures with increasing heat input
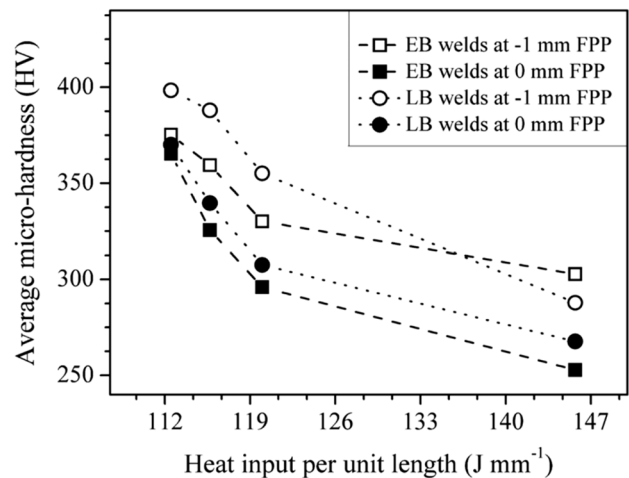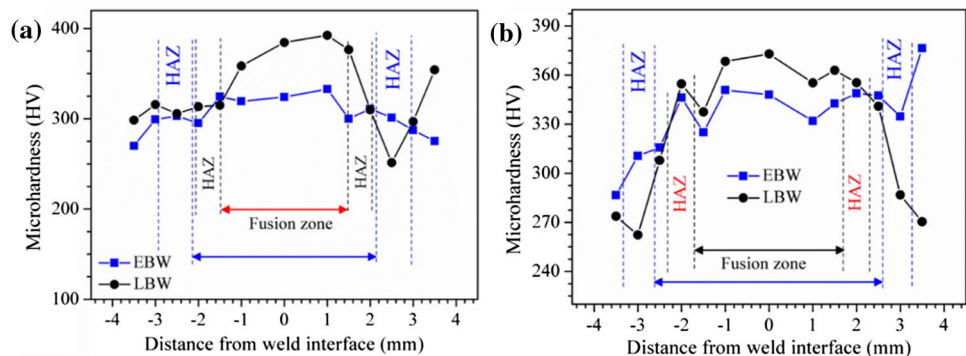
Fig. 10 Average micro-hardness magnitude of laser and electron beam welds at different heat input conditions and FPP

Fig. 9 Vickers micro-hardness profile across the weld joint at 112.5 J mm^{-1} and FPP **a** 0 mm; **b** -1 mm

condition. Strength of the weld joint depends on the strength of martensite α^1 structures. The strength increases with the refinement of α^1 martensitic grain structures. The primary α^1 martensitic grains will exhibit thin and fine needle-like morphology, while weld strength reduces as martensitic grain structures exhibit coarser and plate-like morphology. In the present case, it has been observed that with an increase in heat input condition the martensitic structures exhibited coarse α^1 martensitic structures of plate-like morphology. Similar trend was reported by Wang et al. [21] and Baruah et al. [22]. Moreover, the average micro-hardness value is determined to be higher in laser beam welds than electron beam welds. And, the hardness value is higher in laser and electron beam weldments at negative defocused beam condition due to faster solidification rate.
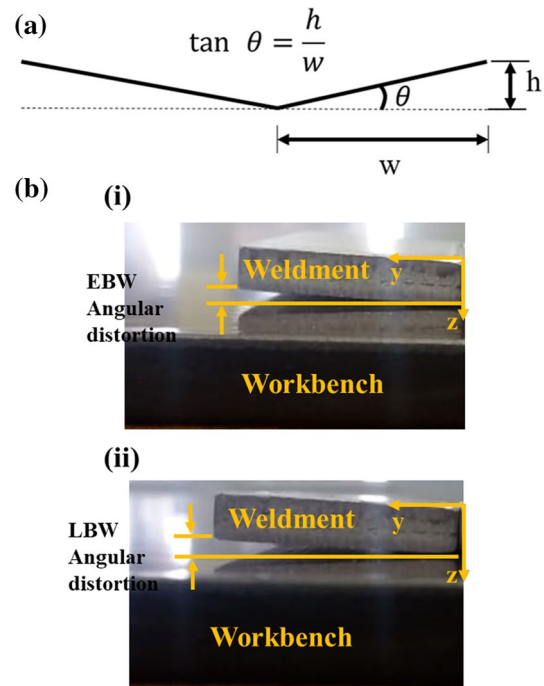
3.3 Welding-induced distortion

The distortion in welding process is associated with generation of nonlinear thermal strains which is evolved due to thermal cycle. In the present work, butt-joint Ti6Al4V alloy plates underwent non-uniform transverse bending (angular deflection) with negligible longitudinal bending. Moreover, from the experimental observation, it is observed that the deformation is concave–concave mode. And, this specific deformation mode is formed only when shrinkage force is relatively lower in longitudinal direction. Figure 11 presents the schematic of angular deflection pattern and welding-induced distortion samples. The angular distortion can be estimated using the following relation

$$\tan\theta = \frac{h}{w} \tag{1}$$

where 'h' and 'w' are the distorted height and width of the weld plate, respectively.

The major driving factors for angular deformation in weldments are solidification shrinkage and thermal contraction in transverse direction. It also depends on difference in fusion zone (FZ) areas above and below the neutral plane. Fundamentally, the magnitude of angular deformation is proportional to high transverse shrinkage and larger difference in FZ areas above and below the neutral axis [22]. Moreover, the transverse shrinkage is quite non-uniform in Ti6Al4V alloy welds since it induces higher shrinkage at the top weld cross section than at the lower weld cross section. Therefore, it can be observed that the weld profile is relatively wider at the top cross section than at the lower cross section (Fig. 4). This also results in upward lift of the weld plate from the weld joint location.

The non-uniform transverse shrinkage across the laser and electron beam weld joint has resulted in angular deflection of concave–concave mode. The average angular


Fig. 11 **a** Schematic of angular deflection pattern and **b** welding-induced distortion samples

deflection of laser and electron beam welds at extreme edge of the weld plates is shown in Fig. 12. The magnitude of angular deflection is increased nominally with increasing heat input condition for both the laser and electron beam welds (Fig. 12a and b). However, the difference in deflection magnitude between laser and electron beam welds at 0 mm FPP and − 1 mm FPP is 78.3% and 77.4%, respectively. The above data infer that the difference in deflection magnitude corresponding to laser and electron beam welds is due to high difference in weld zone areas across the neutral axis.

Moreover, from Fig. 12, it can be observed that the average angular deflection magnitude corresponding to laser beam welds at focused beam and negative defocused beam condition is 4.67° and 3.92°, respectively. Furthermore, the average magnitude of angular deflection for electron beam welds at 0 mm FPP and − 1 mm FPP is 3.97° and 1.04°. This signifies that the angular deflection magnitude in electron beam and laser beam weldments is lowered by 15.8% and 7.4%, respectively, due to negative defocusing beam position. Figure 13 represents the difference in FZ areas above and below the neutral axis corresponding to welding conditions given in Tables 3 and 4. It is observed that a higher difference in FZ area is observed in laser beam welds as compared to electron beam welds. Hence, the angular deflection magnitude is higher for laser beam welds.

Fig. 12 Angular deflection of laser and electron beam welds corresponding to FPP **a** 0 mm and **b** −1 mm
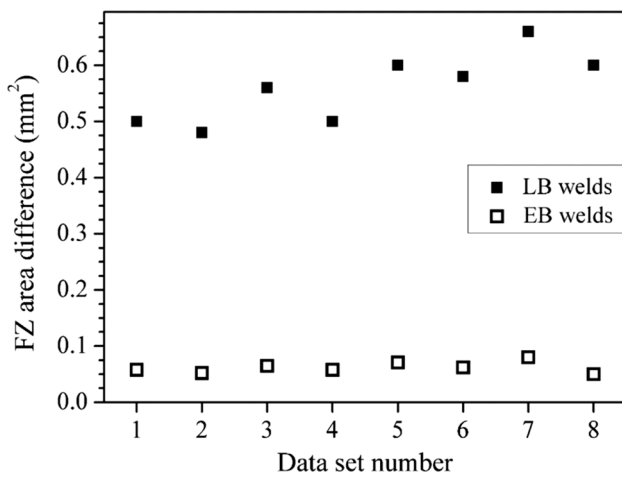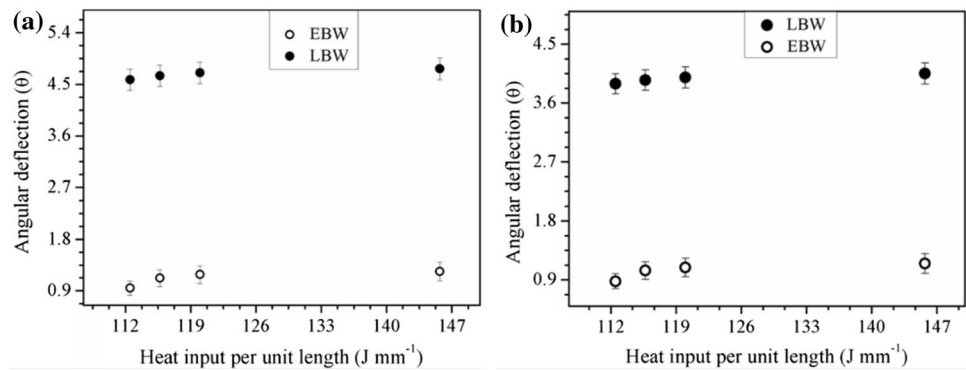
Fig. 13 Difference in FZ areas above and below the neutral axis corresponding to welding conditions given in Tables 3 and 4

4 Conclusions

The influence of fiber laser and electron beam welding processes under same heat input condition and focal point position is examined with respect to physical and microstructural attributes, micro-hardness and angular deflection characteristics. The following conclusions are derived from the present investigation.

(i) Weld penetration and width are significantly lower in laser beam weldments when compared with electron beam weldments. Also, pores are identified at the interfacial boundary of fusion and heat-affected zone of laser beam weldments.

(ii) From microstructural analysis, it is recognized that the electron beam weldments at focused beam condition experience a slower solidification process when compared with laser beam weldments.

(iii) At negative defocused beam condition of laser and electron beam welding processes, refined α^1 crystals of lower width are evolved in the fusion zone. However, coarser and elongated α^1 structure along with higher fraction content of retained β phase is formed in the weld zone of Ti6Al4V alloy samples at higher heat input condition.

(iv) Negative defocusing of beam position has improved the micro-hardness magnitude by 32% and 16% in laser and electron beam weldments, respectively.

(v) The laser beam weldments displayed a higher angular deflection magnitude when compared with electron beam weldments on account of higher difference in fusion zone areas across the neutral axis. However, by defocusing the beam position by -1 mm the angular deflection magnitude is lowered by 15.8% and 7.4% in laser and electron beam weldments, respectively.

References

1. Beranoagirre A, Olvera D, De Lacalle LL (2012) Milling of gamma titanium–aluminum alloys. Int J Adv Manuf Technol 62:83–88. https://doi.org/10.1007/s00170-011-3812-6

2. Short AB (2009) Gas tungsten arc welding of α+ β titanium alloys: a review. Mater Sci Technol 25(3):309–324. https://doi.org/10.1179/174328408X389463

3. Kumar C, Das M, Paul CP, Bindra KS (2018) Characteristics of fiber laser weldments of two phases (α+ β) titanium alloy. J Manuf Process 35:351–359. https://doi.org/10.1016/j.jmapro.2018.08.023

4. Li Z, Rostam K, Panjehpour A, Akbari M, Karimipour A, Rostami S (2020) Experimental and numerical study of temperature field and molten pool dimensions in dissimilar thickness laser

welding of Ti6Al4V alloy. J Manuf Process 49:438–446. https://doi.org/10.1016/j.jmapro.2019.11.024

5. Ning J, Hong KM, Inamke GV, Shin YC, Zhang LJ (2019) Analysis of microstructure and mechanical strength of lap joints of TZM alloy welded by a fiber laser. J Manuf Process 39:146–159. https://doi.org/10.1016/j.jmapro.2019.02.015

6. Li L, Wang S, Huang W, Jin Y (2020) Microstructure and mechanical properties of electron beam welded TC4/TA7 dissimilar titanium alloy joint. J Manuf Process 50:295–304. https://doi.org/10.1016/j.jmapro.2019.11.007

7. Jikang F, Zhang W, Bojin Q, Fangjun L (2017) Influence of multi-beam electron beam welding technique on the deformation of Ti6Al4V alloy sheet. Rare Metal Mater Eng 46(9):2417–2422. https://doi.org/10.1016/S1875-5372(17)30208-4

8. Huang A, Zhang J, Gao C, Hu R, Pang S (2019) Effects of groove constraint space on plasma characteristics during Laser-MIG hybrid welding of Titanium alloy. J Manuf Process 48:137–144. https://doi.org/10.1016/j.jmapro.2019.11.004

9. Zhou L, Yu M, Hongyun Z, Zhihua J, Fan G, Xiaoguo S (2019) Dissimilar friction stir welding of AA6061 and Ti6Al4V alloys: A study on microstructure and mechanical properties. J Manuf Proces 48:119–126. https://doi.org/10.1016/j.jmapro.2019.09.043

10. Maio L, Liberini M, Campanella D, Astarita A, Esposito S, Boccardi S, Meola C (2017) Infrared thermography for monitoring heat generation in a linear friction welding process of Ti6Al4V alloy. Infrared Phy Technol 81:325–338. https://doi.org/10.1016/j.infrared.2017.01.023

11. Yunlian Q, Ju D, Quan H, Liying Z (2000) Electron beam welding, laser beam welding and gas tungsten arc welding of titanium sheets. Mater Sci Eng A 280(15):177–181. https://doi.org/10.1016/S0921-5093(99)00662-0

12. Gao XL, Zhang L, Liu J, Zhang JX (2013) A comparative study of pulsed Nd:YAG laser welding and TIG welding of thin Ti6Al4V titanium alloy plate. Mater Sci Eng A 559(1):14–21. https://doi.org/10.1016/j.msea.2012.06.016

13. Suresh DM, Mohandas T (2010) A comparative evaluation of friction and electron beam welds of near-α titanium alloy. Mater Desig 31(4):2245–2252. https://doi.org/10.1016/j.matdes.2009.10.012

14. Ruifeng L, ZhuGuo L, Yanyan Z, Lei R (2011) A comparative study of laser beam welding and laser-MIG hybrid welding of Ti-Al-Zr-Fe titanium alloy. Mater Sci Eng A 528(3):1138–1142. https://doi.org/10.1016/j.msea.2010.09.084

15. Klimpel A, Lisiecki A (2007) Laser welding of butt joints of austenitic stainless steel AISI 321. J Achievements Mater Manuf Eng 25(1):63–66

16. Saresh N, Pillai MG, Mathew J (2007) Investigations into the effects of electron beam welding on thick Ti-6Al-4V titanium alloy. J Mater Proces Technol 192–193:83–88. https://doi.org/10.1016/j.jmatprotec.2007.04.048

17. Katayama S (2013) Handbook of laser welding technologies. Woodhead Publishing Limited, Sawston

18. Kabir ASH, Cao X, Medraj M, Wanjara P, Cuddy J, Birur A (2010) Effect of welding speed and defocusing distance on the quality of laser welded Ti-6Al-4V. Materials Science & Technology 2010 Conference and Exhibition, pp 2787–2797. Accessed 25 January 2020, from https://www.asminternational.org/home/-/journal_content/56/10192/CP2010MST2787/CONFERENCE-PAPER#main-content

19. Li S, Chen Y, Kang J, Huang Y, Gianetto JA, Yin L (2019) Interfacial microstructures and mechanical properties of dissimilar titanium alloy and steel friction stir butt-welds. J Manuf Process 40:160–168. https://doi.org/10.1016/j.jmapro.2019.03.015

20. Li Y, Zhao Y, Li Q, Wu A, Zhu R, Wang G (2017) Effects of welding condition on weld shape and distortion in electron beam welded Ti2AlNb alloy joint. Mater Design 114:226–233. https://doi.org/10.1016/j.matdes.2016.11.083

21. Wang S, Wu X (2012) Investigation on the microstructure and mechanical properties of Ti–6Al–4V alloy joints with electron beam welding. Mater Design 36:663–670. https://doi.org/10.1016/j.matdes.2011.11.068

22. Baruah M, Bag S (2016) Microstructural influence on mechanical properties in plasma microwelding of ti6al4v alloy. J Mater Eng Perform 25:4718–4728. https://doi.org/10.1007/s11665-016-2333-8